Available online at www.sciencedirect.com
ScienceDirect
Journal of Applied Geophysics 62 (2007) 193–203
JOURNAL OF APPLIED GEOPHYSICS
www.elsevier.com/locate/jappgeo

Simulation of upscaling effects due to wave-induced fluid flow in Biot media using the finite-element method

J. Germán Rubino [a,*], Juan E. Santos [a,b], Stefano Picotti [c], José M. Carcione [c]

[a] C.O.N.I.C.E.T., Facultad de Ciencias Astronómicas y Geofísicas, Universidad Nacional de La Plata, Paseo del Bosque, S/N, (1900) La Plata, Argentina
[b] Department of Mathematics, Purdue University, 150 N. University Street, West Lafayette, Indiana, 47907-2067, USA
[c] Istituto Nazionale di Oceanografia e di Geofisica Sperimentale (OGS) Borgo Grota Gigante 42c, 34010, Sgonico, Trieste, Italy

Received 24 August 2006; accepted 6 November 2006

Abstract

An important upscaling effect in heterogeneous poroelastic Biot media is the dissipation mechanism due to wave-induced fluid flow caused by mesoscopic scale heterogeneities. A typical mesoscopic heterogeneity has a size of tens of centimeters and can be due to local variations in lithological properties or to patches of immiscible fluids. For example, a fast compressional wave traveling across a porous rock saturated with water and patches of gas induces a greater fluid pressure in the gas patches than in the water saturated parts of the material. This in turn generates fluid flow and slow Biot waves which diffuse away from the gas–water interfaces generating significant losses in the seismic range. In this work an iterative domain-decomposition finite-element procedure is presented and employed to simulate this type of upscaling effects in alternating layers of poroelastic rock saturated with either gas or water. The domain-decomposition procedure is naturally parallelizable, which is a necessity in this type of simulations due to the large number of degrees of freedom needed to accurately represent these attenuation effects. The numerical simulations were designed to show the effects of the wave-induced fluid flow on the traveling waves. Our results are the first numerical evidence of the mesoscopic loss mechanism in the seismic range of frequencies for this type of porous heterogeneous media.
© 2006 Elsevier B.V. All rights reserved.

Keywords: Wave-induced fluid flow; Poroelasticity; Finite elements; Seismic attenuation; Phase velocity

1. Introduction

The propagation of waves in a porous elastic solid saturated by a single-phase compressible viscous fluid was first analyzed by Biot in several classical papers (Biot, 1956a,b, 1962). Biot assumed that the fluid may flow relative to the solid frame causing friction. Biot also predicted the existence of two compressional waves, denoted here as P1 and P2 compressional waves, and one shear or S wave. The three waves undergo attenuation and dispersion effects in the seismic to the ultrasonic range of frequencies. The P1 and shear waves have a behavior similar to that in an elastic solid, with high phase velocities, low attenuation and very little dispersion. The P2 wave behaves as a diffusion-type wave due to its low phase velocity and very high attenuation and dispersion. One important cause of attenuation at seismic frequencies in fluid-saturated porous media is wave-induced fluid

* Corresponding author. Tel.: +54 221 4236593; fax: +54 221 4236591.
E-mail addresses: grubino@fcaglp.fcaglp.unlp.edu.ar (J.G. Rubino), santos@fcaglp.fcaglp.unlp.edu.ar (J.E. Santos), spicotti@ogs.trieste.it (S. Picotti), jcarcione@ogs.trieste.it (J.M. Carcione).

0926-9851/$ - see front matter © 2006 Elsevier B.V. All rights reserved.
doi:10.1016/j.jappgeo.2006.11.003

Table 1
Material properties of the system

Solid matrix	Solid grains bulk modulus, K_s	37 GPa
	Dry matrix bulk modulus, K_m	8 GPa
	Dry matrix shear modulus, μ	9.5 GPa
	Solid grains density, ρ_s	2650 kg/m^3
Water	Bulk modulus, K_f	2.25 GPa
	Density, ρ_f	1040 kg/m^3
	Viscosity, η	0.003 Pa s
Gas	Bulk modulus, K_f	0.012 GPa
	Density, ρ_2	78 kg/m^3
	Viscosity, η	0.00015 Pa s

flow at mesoscopic scale heterogeneities, which are those larger than pore size but smaller than wavelengths in the seismic range (1–100 Hz). As pointed out by White (White et al., 1975), sometimes gas saturation over a large vertical section occurs in thin layers, separated by liquid-saturated layers. This is the simplest case of mesoscopic heterogeneities and White showed that in this case fluid flow effects add up and play a major role. Numerical simulations to analyze attenuation effects in an homogeneous sandstone saturated with brine and spherical gas pockets at laboratory frequencies were presented by Carcione et al. (2003) and Helle et al. (2003).

In this article we describe the use of a parallel iterative finite-element domain-decomposition procedure to simulate the propagation of waves in laminated porous media in the seismic range of frequencies. The algorithm employs the nonconforming rectangular element defined by Douglas et al. (1999) to approximate the displacement vector in the solid phase. The dispersion analysis presented by Zyserman et al. (2003) shows that using this nonconforming element allows for a reduction in the number of points per wavelength necessary to reach a desired accuracy. It is also the case that the use of nonconforming

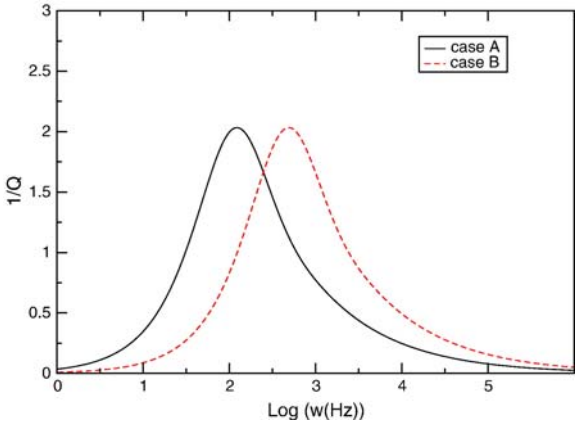


Fig. 1. Inverse of the quality factor $Q(\omega)$ for a sandstone saturated with water and gas for cases A and B.

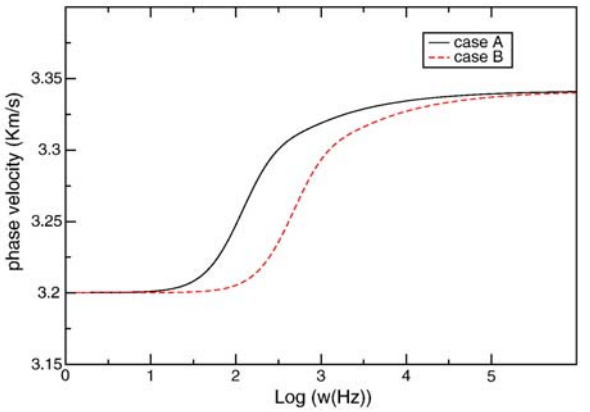


Fig. 2. Phase velocity $c_p(\omega)$ for a sandstone saturated with water and gas for cases A and B.

elements reduces the amount of information that needs to be exchanged in any parallel implementation of the algorithm, as compared with the corresponding procedure using conforming elements of the same order. The displacement in the fluid phase is approximated using the vector part of the Raviart–Thomas–Nedelec mixed finite-element space of zero order, which is a conforming space (Raviart and Thomas, 1975; Nedelec, 1980). The convergence analysis of this type of iterative algorithm was presented by Santos and Sheen (in press). The numerical experiments were run in the IBM SP2 and the community cluster parallel computers at Purdue University under the MPI standards. The simulations show clearly the mesoscopic loss mechanism due to the wave-induced fluid flow, and the observed attenuation is in very good agreement with that predicted by the White theory.

2. Review of Biot theory

We consider a porous solid saturated by a single phase, compressible viscous fluid and assume that the whole aggregate is isotropic. Let $u^s=(u_i^s)$ and $\tilde{u}^f=(\tilde{u}_i^f)$, $i=1, \ldots, d$ denote the averaged displacement vectors of the solid and fluid phases, respectively, where d denotes the Euclidean dimension. Also let

$$u^f = \phi(\tilde{u}^f - u^s),$$

be the average relative fluid displacement per unit volume of bulk material, where ϕ denotes the effective porosity. Set $u=(u^s, u^f)$ and note that

$$\xi = -\nabla \cdot u^f,$$

represents the change in fluid content.

Let ε_{ij} (u^s) be the strain tensor of the solid. Also, let σ_{ij}, $i, j=1, \ldots, d$, and p_f denote the stress tensor of the bulk material and the fluid pressure, respectively. Following Biot (1962), the stress–strain relations can be written in the form:

$$\sigma_{ij}(u) = 2\mu\varepsilon_{ij}(u^s) + \delta_{ij}(\lambda_c \nabla \cdot u^s - \alpha K_{av}\xi), \tag{2.1a}$$

$$p_f(u) = -\alpha K_{av} \nabla \cdot u^s + K_{av}\xi. \tag{2.1b}$$

The coefficient μ is equal to the shear modulus of the bulk material, considered to be equal to the shear modulus of the dry matrix. Also

$$\lambda_c = K_c - \frac{2}{d}\mu,$$

with K_c being the bulk modulus of the saturated material. Following Santos et al. (1992) and Gassmann (1951), the coefficients in Eqs. (2.1a), (2.1b) can be obtained from the relations

$$\alpha = 1 - \frac{K_m}{K_s},\ K_{av} = \left(\frac{\alpha-\phi}{K_s} + \frac{\phi}{K_f}\right)^{-1}, K_c = K_m + \alpha^2 K_{av}, \tag{2.2}$$

where K_s, K_m and K_f denote the bulk modulus of the solid grains composing the solid matrix, the dry matrix and the saturant fluid, respectively. The coefficient α is known as the effective stress coefficient of the bulk material.

2.1. The equations of motion

Let us consider an open bounded domain $\Omega \subset R^d$ of bulk material with boundary $\Gamma = \partial\Omega$. Let ρ_s and ρ_f denote the mass densities of the solid grains and the fluid and let

$$\rho_b = (1-\phi)\rho_s + \phi\rho_f$$

denote the mass density of the bulk material. Let the positive definite matrix $\mathcal{P}$ and the nonnegative matrix $\mathcal{B}$ be defined by

$$\mathcal{P} = \begin{pmatrix} \rho_b I & \rho_f I \\ \rho_f I & gI \end{pmatrix}, \quad \mathcal{B} = \begin{pmatrix} 0I & 0I \\ 0I & bI \end{pmatrix}.$$

Here I denotes the identity matrix in $R^{d\times d}$. The mass coupling coefficient g represents the inertial effects associated with dynamic interactions between the solid and fluid phases, while the coefficient b includes the viscous coupling effects between such phases. They are given by the relations

$$b = \frac{\eta}{k}, \quad g = \frac{S\rho_f}{\phi}, \quad S = \frac{1}{2}\left(1 + \frac{1}{\phi}\right), \tag{2.3}$$

where η is the fluid viscosity and k the absolute permeability. S is known as the structure or tortuosity factor. Next, let $\mathcal{L}(u)$ be the second order differential operator defined by

$$\mathcal{L}(u) = (\nabla \cdot \sigma(u), -\nabla p_f(u))^t.$$

Then if $\omega = 2\pi f$ is the angular frequency and $F(x, \omega) = (F^s(x, \omega), F^f(x, \omega))$ is the external source, the equations of motion, stated in the space–frequency domain, are (see Biot, 1956a,b)

$$-\omega^2 \mathcal{P}u(x,\omega) + i\omega\mathcal{B}u(x,\omega) - \mathcal{L}(u(x,\omega)) = F(x,\omega),\ x \in \Omega. \tag{2.4}$$

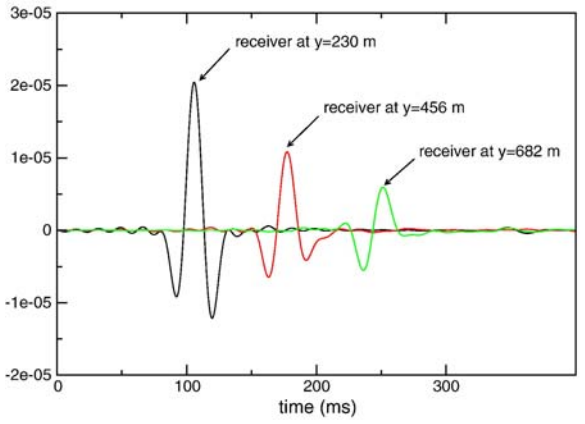


Fig. 3. Vertical component of the particle velocity of the solid phase as a function of time for the periodic gas–water saturated porous medium of case A.

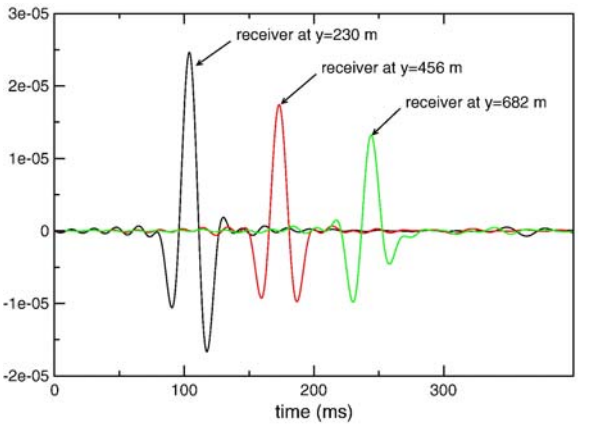


Fig. 4. Vertical component of the particle velocity of the solid phase as a function of time for the water-saturated porous medium related to case A.

It was shown by Biot (1956a,b) that two compressional waves, denoted here as P1 and P2, and one shear or S wave can propagate. The P1 and S waves correspond to the classical compressional and shear waves propagating in elastic or viscoelastic isotropic solids. The additional P2 slow mode is a wave strongly attenuated in the low frequency range, associated with the motion out of phase of the solid and fluid phases.

Let us state a boundary condition needed to completely define our differential model. Denote by ν the unit outer normal on Γ. In the 2D case let χ be a unit tangent on Γ so that $\{\nu, \chi\}$ is an orthonormal system on Γ. In the 3D case let χ^1 and χ^2 be two unit tangents on Γ so that $\{\nu, \chi^1, \chi^2\}$ is an orthonormal system on Γ. Then, in the 2D case set

$$\mathcal{G}_\Gamma(u) = (\sigma(u)\nu\cdot\nu, \sigma(u)\nu\cdot\chi, p_{\mathrm{f}}(u))^t, \tag{2.5}$$

$$S_\Gamma(u) = (u^{\mathrm{s}}\cdot\nu, u^{\mathrm{s}}\cdot\chi, u^{\mathrm{f}}\cdot\nu)^t,$$

and in the 3D case set

$$\mathcal{G}_\Gamma(u) = \left(\sigma(u)\nu\cdot\nu, \sigma(u)\nu\cdot\chi^1, \sigma(u)\nu\cdot\chi^2, p_{\mathrm{f}}(u)\right)^t, \tag{2.6}$$

$$S_\Gamma(u) = (u^{\mathrm{s}}\cdot\nu, u^{\mathrm{s}}\cdot\chi^1, u^{\mathrm{s}}\cdot\chi^2, u^{\mathrm{f}}\cdot\nu)^t.$$

Let us consider the solution of Eq. (2.4) with the following absorbing boundary condition

$$-\mathcal{G}_\Gamma(u(x,\omega)) = i\omega\mathcal{D}S_\Gamma(u(x,\omega)), \quad x\in\Gamma. \tag{2.7}$$

The matrix $\mathcal{D}$ in Eq. (2.7) is positive definite. In the 2D case it is given by the following relations, with the obvious extension to the 3D case: $\mathcal{D} = \mathcal{A}^{\frac{1}{2}}\mathcal{N}^{\frac{1}{2}}\mathcal{A}^{\frac{1}{2}}$, where $\mathcal{N} = \mathcal{A}^{-\frac{1}{2}}\mathcal{M}^{\frac{1}{2}}\mathcal{A}^{-\frac{1}{2}}$ and

$$\mathcal{A} = \begin{pmatrix} \rho_{\mathrm{b}} & 0 & \rho_{\mathrm{f}} \\ 0 & \rho_{\mathrm{b}} - \dfrac{(\rho_{\mathrm{f}})^2}{g} & 0 \\ \rho_{\mathrm{f}} & 0 & g \end{pmatrix}, \tag{2.8}$$

$$\mathcal{M} = \begin{pmatrix} \lambda_{\mathrm{c}} + 2\mu & 0 & \alpha K_{\mathrm{av}} \\ 0 & \mu & 0 \\ \alpha K_{\mathrm{av}} & 0 & K_{\mathrm{av}} \end{pmatrix}.$$

2.2. A variational formulation

In order to state a variational formulation for Eqs. (2.4) and (2.7) we need to introduce some notation. For $X\subset R^d$ with boundary ∂X, let $(\cdot,\cdot)_X$ and $\langle\cdot,\cdot\rangle_{\partial X}$ denote the complex $L^2(X)$ and $L^2(\partial X)$ inner products for scalar, vector, or matrix valued functions. Also, for $s\in R$, $\|\cdot\|_{s,X}$ and $|\cdot|_{s,X}$ will denote the usual norm and seminorm for the Sobolev space $H^s(X)$. In addition, if $X=\Omega$ or $X=\Gamma$, the subscript X may be omitted such that $(\cdot,\cdot)=(\cdot,\cdot)_\Omega$ or $\langle\cdot,\cdot\rangle=\langle\cdot,\cdot\rangle_\Gamma$. Also, set

$$H(\mathrm{div};\Omega) = \{\upsilon \in [L^2(\Omega)]^d : \nabla\cdot\upsilon\in L^2(\Omega)\},$$

$$H^1(\mathrm{div};\Omega) = \{\upsilon\in[H^1(\Omega)]^d : \nabla\cdot\upsilon\in H^1(\Omega)\},$$

with the norms

$$||\upsilon||_{H(\mathrm{div};\Omega)} = [||\upsilon||_0^2 + ||\nabla\cdot\upsilon||_0^2]^{1/2};$$

$$||\upsilon||_{H^1(\mathrm{div};\Omega)} = [||\upsilon||_1^2 + ||\nabla\cdot\upsilon||_1^2]^{1/2}.$$

Let us introduce the space $\mathcal{V} = [H^1(\Omega)]^d \times H(\mathrm{div};\Omega)$. Then multiply Eq. (2.4) by $\upsilon\in\mathcal{V}$, use integration by parts and apply the boundary condition (2.7) to see that the solution u of Eqs. (2.4) and (2.7) satisfies *the weak form*:

$$\begin{aligned} &-\omega^2(\mathcal{P}u,\upsilon) + i\omega(\mathcal{B}u,\upsilon) + \sum_{l,m}(\tau_{\mathrm{lm}}(u), \varepsilon_{\mathrm{lm}}(\upsilon^{(1)})) \\ &-(p_{\mathrm{f}}(u), \nabla\cdot\upsilon^{(2)}) + i\omega\langle\mathcal{D}\,S_\Gamma(u),\ S_\Gamma\upsilon\rangle = (F,\upsilon), \\ &\qquad \upsilon = (\upsilon^{(1)},\upsilon^{(2)})^t\in\mathcal{V}. \end{aligned} \tag{2.9}$$

The argument presented by Santos and Sheen (in press) for a generalized composite Biot model can be used here to show that problem (2.9) has a unique solution for any $\omega\neq 0$.

3. Simulation techniques

In order to analyze the attenuation effect due to wave-induced fluid flow, Eq. (2.9) was solved in a rectangular poroelastic domain Ω in the (x, y)-plane. Let $\mathcal{T}^h(\Omega)$ be a non-overlapping partition of Ω into rectangles Ω_j of diameter bounded by h such that $\overline{\Omega} = \cup_{j=1}^J \overline{\Omega}_j$.

Two different finite-element spaces associated with the partition $\mathcal{T}^h(\Omega)$ were employed to discretize the solid and fluid displacement vectors. Each component of the solid displacement vector was approximated using the 2D non-conforming finite-element space $\mathcal{N}C^h$ presented in Douglas et al. (1999), while to approximate the fluid displacement the vector part of the Raviart–Thomas–Nedelec space (Raviart and Thomas, 1975; Nedelec, 1980) of zero order, denoted $\mathcal{W}^h$, was chosen. Appendix A describes these finite-element spaces and their approximation properties.

Then, if $\mathcal{V}^h = (\mathcal{N}C^h)^2 \times \mathcal{W}^h$, the *global* finite-element procedure is defined as follows: find $u^h=(u^{(1,h)}, u^{(2,h)})^t \in \mathcal{V}^h$ such that

$$-\omega^2(\mathcal{P}u^h, \upsilon) + i\omega(\mathcal{B}u^h, \upsilon) + \sum_j [(\sigma_{\mathrm{lm}}(u), \varepsilon_{\mathrm{lm}}(\upsilon^{(1)}))_{\Omega_j} - (p_{\mathrm{f}}(u), \nabla \cdot \upsilon^{(2)})_{\Omega_j}] + i\omega\langle \mathcal{D}\, S_\Gamma(u^h),\ S_\Gamma(\upsilon)\rangle = (F, \upsilon),\ \upsilon = (\upsilon^{(1)}, \upsilon^{(2)})^t \in \mathcal{V}^h. \quad (3.1)$$

To perform the numerical simulations needed to represent the mesoscopic loss mechanism, the computer implementation of the global procedure (3.1) would require the solution of a huge linear system of equations due to the large number of degrees of freedom needed to represent the phenomenon. Since the algebraic problem associated with Eq. (3.1) is complex valued and non-coercive, no known efficient iterative global solvers can be employed. To tackle this problem, a parallel iterative domain-decomposition algorithm was employed as described in Appendix A.

4. Numerical example

We consider wave propagation in a poroelastic medium Ω of uniform porosity $\phi=0.3$ and permeability $k=0.986923\ 10^{-12}$ m^2, saturated with either gas or water. The value of the structure factor S in Eq. (2.3) was chosen to be 1. The other material properties of the system are given in Table 1. The domain Ω is a square of side length L divided into two subdomains Ω_{homo} and Ω_{per}.

In case A, $L=800$ m and $\Omega_{\mathrm{homo}}=\{0<x<800$ m, $0<y<8.8$ m$\}$, $\Omega_{\mathrm{per}}=\{0\le x\le 800$ m, $8.8<y<800$ m$\}$, while in case B, $L=320$ m and $\Omega_{\mathrm{homo}}=\{0<x<320$ m, $0<y<4.4$ m$\}$, $\Omega_{\mathrm{per}}=\{0\le x<320$ m, $4.4<y<320$ m$\}$.

In both cases the region Ω_{homo} is fully saturated with water, while the region Ω_{per} consists of horizontal layers of width 0.4 m for case A and 0.2 m for case B, alternatively saturated with either gas or water.

In order to analyze the mesoscopic loss mechanism it is convenient first to approximate the saturated porous medium Ω by a viscoelastic solid and use the concept of complex velocity as follows (see, for example, Carcione, 2001). Recall that in a viscoelastic solid, the quality factor $Q(\omega)$ is defined by the relation

$$Q(\omega) = \frac{\mathrm{Re}(\upsilon_{\mathrm{p}}^2)}{\mathrm{Im}(\upsilon_{\mathrm{p}}^2)},$$

where υ_{p} is the complex compressional velocity given by

$$\upsilon_{\mathrm{p}}(\omega) = \sqrt{\frac{E}{\overline{\rho}_{\mathrm{b}}}}. \quad (4.1)$$

In Eq. (4.1) $\overline{\rho}_{\mathrm{b}}$ is the average bulk density over Ω and $E=E(\omega)=|E|e^{i\theta}$ is the complex plane wave modulus associated with the domain Ω as defined by White et al. (1975), which complicated expression involving all coefficients in Biot's equations of motion (2.4) is included in Appendix B.

The quality factor is related to the loss angle θ by the formula

$$Q^{-1}(\omega) = \tan\theta.$$

Fig. 1 displays the inverse of the quality factor $Q(\omega)$ for both cases, showing that the minimum value of $Q(\omega)$ is approximately equal to 28 for cases A and B, corresponding to the frequencies 20 Hz and 77 Hz for cases A and B, respectively. These frequencies were chosen as the dominant frequencies of the external source to be used in our numerical simulations, which allowed us to better visualize the attenuation effects being analyzed.

Fig. 2 shows the phase velocities $c_{\mathrm{p}}(\omega)$ for both cases, obtained from the expression

$$c_{\mathrm{p}}(\omega) = \left[\mathrm{Re}\left(\frac{1}{\upsilon_{\mathrm{p}}(\omega)}\right)\right]^{-1},$$

where it can be observed the velocity dispersion associated with the wave-induced fluid flow mechanism.

The source function $(F^{\mathrm{s}}, F^{\mathrm{f}})$ is a compressional point source located inside the region Ω_{homo} at $(x_{\mathrm{s}}, y_{\mathrm{s}})=(400$ m, 4 m) for case A and at $(x_{\mathrm{s}}, y_{\mathrm{s}})=(160$ m, 4 m) for case B, applied to the solid frame. It has the form

$$F^{\mathrm{s}}(x,y,\omega) = \nabla\delta_{x_{\mathrm{s}},y_{\mathrm{s}}}\mathrm{g}(\omega), \qquad F^{\mathrm{f}} = 0,$$

where $\delta_{x_{\mathrm{s}},y_{\mathrm{s}}}$ ydenotes the Dirac distribution at $(x_{\mathrm{s}}, y_{\mathrm{s}})$. Also, $g(\omega)$ is the Fourier transform of the waveform

$$\mathrm{g}(t) = -2\xi(t-t_0)e^{-\xi(t-t_0)^2},$$

with $\xi=8f_0^2$, $t_0=1.25/f_0$, where the value f_0 was chosen such that the source central (dominant) frequency be equal to 20 Hz for case A and 77 Hz for case B.

The parallel iterative procedure (A.3a)–(A.3b) described in Appendix A was used to find the time Fourier transforms of the displacement vectors of the solid and fluid phases for 110 equally spaced temporal

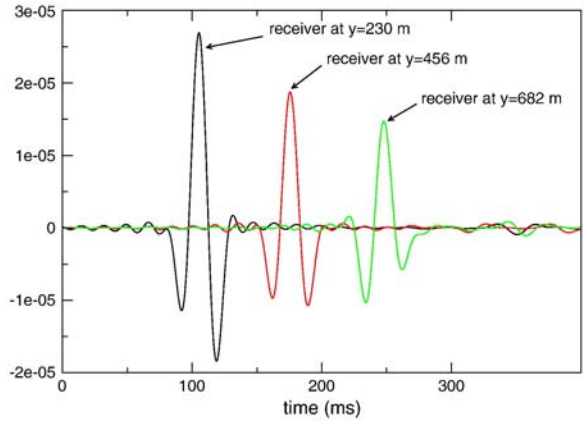


Fig. 5. Vertical component of the particle velocity of the solid phase as a function of time for the gas-saturated porous medium related to case A.

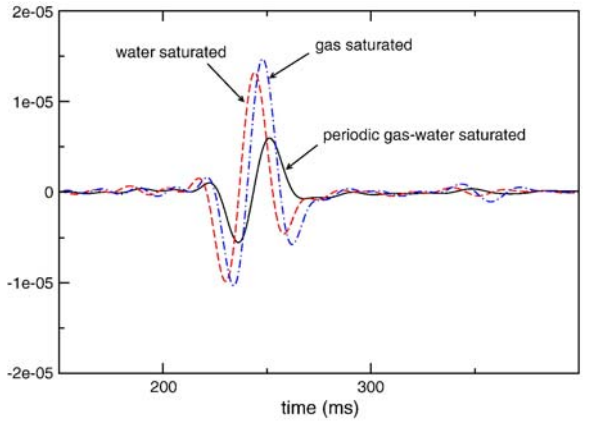


Fig. 6. Vertical component of the particle velocity of the solid phase as a function of time at receiver r_3 located at $x=400$ m, $y=682$ m for the periodic gas–water case A and the related water and gas saturated experiments, respectively.

frequencies in the interval (0, 60 Hz) for case A and (0, 242 Hz) for case B. The algorithm was implemented employing a uniform partition $\mathcal{T}^h$ of Ω into squares of side length $h=0.4$ m for case A and $h=0.2$ m for case B. The time domain solution was obtained after performing an approximate inverse Fourier transform. The numerical experiments were run in the IBM SP2 and the community cluster parallel computers at Purdue University under the MPI standard. To better observe the mesoscopic attenuation effects, in case A we also run the same experiment but when the subdomain Ω_{per} is fully saturated with either water or gas.

Figs. 3, 4, and 5 show the vertical component of the particle velocity of the solid phase as a function of time, for the case A and the corresponding homogeneous experiments, i.e., the periodic gas–water saturated case A, and the homogeneous water and gas saturated experiments, at three receivers r_j with receiver locations (x_{rj}, y_{rj}), $j=1, 2, 3$, where $x_{rj}=400$ m, $j=1, 2, 3$ and $y_{r1}=230$ m, $y_{r2}=456$ m, $y_{r3}=682$ m.

The amplitude peaks corresponding to the arrival of the fast P1 wave for the case of periodic gas–water saturation are lower than the corresponding peaks for the cases of homogeneous water saturation in Fig. 4 and of homogeneous gas saturation in Fig. 5, showing clearly the mesoscopic loss mechanism predicted by White et al. (1975). This effect is more easily observed in Fig. 6, where the vertical component of the particle velocity of the solid phase at the receiver r_3 is shown for the periodic gas–water case and for the homogeneous water and gas experiments. Note also the delay in the arrival time of the pulse for the periodic case as compared with the homogeneous experiments, showing the velocity dispersion effects caused by the mesoscopic scale heterogeneities.

Notice that the decay rate of the peaks associated with the arrival of the fast P1 wave in Fig. 3 is much larger than the corresponding decay rates in Figs. 4 and 5, which are associated only with geometrical spreading effects. The fast decay rate of the peak amplitudes in Fig. 3 is then caused by the wave-induced fluid flow between the gas and water layers.

Fig. 7 shows the vertical component of the particle velocity of the solid phase as a function of time for case B at three receivers r_j, with receiver locations (x_{rj}, y_{rj}), $j=1, 2, 3$, where $x_{rj}=160$ m, $j=1, 2, 3$ and $y_{r1}=49$ m, $y_{r2}=139$ m, $y_{r3}=229$ m. This figure shows again the fast decay rate in the peak amplitudes associated with the fast P1 arrivals, due to the wave-induced fluid flow mechanism. The corresponding homogeneous experiments

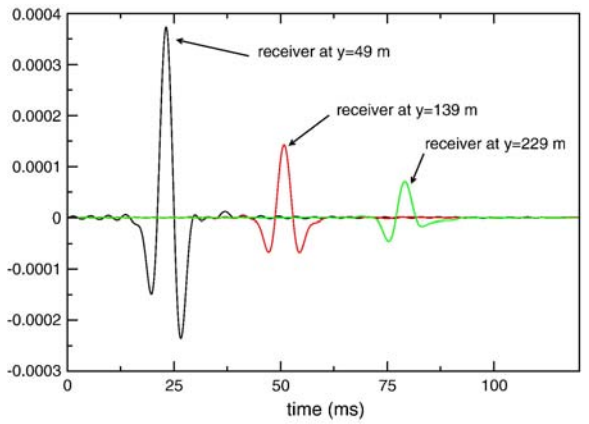


Fig. 7. Vertical component of the particle velocity of the solid phase as a function of time for the periodic gas–water saturated porous medium of case B.

behave in a similar way to case A and the figures are not included here for brevity.

The quality factor $Q(\omega)$ associated with this decay rate can also be evaluated by using the frequency-shift and spectral-ratio methods. Here we briefly describe these procedures. Let $A(f, r_s)$ be the value of the amplitude spectrum of the vertical component of the displacement of the solid phase (as a function of time), observed at the receiver r_s located at a distance d_s from the source at the frequency $f=\omega/2\pi$. Let f_s be the centroid of $A(f, r_s)$, defined by the formula

$$f_s = \frac{\int_o^\infty fA(f, r_s)\mathrm{d}f}{\int_o^\infty A(f, r_s)\mathrm{d}f}.$$

The frequency-shift method analyzed by Quan and Harris (1997) relates the quality factor Q with the centroid frequencies f_s and f_t of two receivers r_s and r_t, respectively, considering the signal at the receiver r_s as the source for the receiver r_t. For the special case when the amplitude spectrum of the signal $A(f, r_s)$ at the receiver r_s is Gaussian with variance σ_s^2, the following equality holds (Quan and Harris, 1997)

$$\frac{\pi(d_t - d_s)}{Qc_p} = (f_s - f_t)/\sigma_s^2, \tag{4.2}$$

where c_p is the average compressional phase velocity in a region containing the receivers r_s and r_t in the frequency band of interest. The value of c_p was estimated from the arrival times at the corresponding receivers.

Another procedure to estimate the quality factor Q is the spectral-ratio method as described by Carcione et al. (2003). The method uses the following relation between the amplitude spectrum of two receivers r_s and r_t (Carcione et al., 2003):

$$\ln\left[\frac{A(\omega, r_s)}{A(\omega, r_t)}\right] = \frac{\omega}{c_p Q}(d_t - d_s) + \ln\left(\frac{G_s}{G_t}\right), \tag{4.3}$$

where G_s and G_t are the corresponding geometrical spreading factors, assumed to be independent of the frequency ω. Thus, the quality factor Q can be determined from the slope of the line fitting $\ln(A(\omega, r_s)/A(\omega, r_t))$.

Table 2
Estimated Q using the frequency-shift and spectral-ratio methods

Source	Receiver	Frequency-shift method	Spectral-ratio method
r_1	r_2	29.96	22.52
r_1	r_3	28	21.71
r_2	r_3	24.63	20.96

Case A.

Table 3
Estimated Q using the frequency-shift and spectral-ratio methods

Source	Receiver	Frequency-shift method	Spectral-ratio method
r_1	r_2	28.33	30.45
r_1	r_3	25.32	24.79
r_2	r_3	22.21	20.9

Case B.

Picotti and Carcione (2006) compare the performances of the two Q-evaluation methods, and show how to use them in the case of noisy signal.

Tables 2 and 3 show the estimated values of Q using the two methods. The Q-estimates are in very good agreement with the theoretical value ($Q=28$ for cases A and B) of the quality factor predicted by White et al. (1975) as shown in Fig. 1.

5. Conclusions

Numerical experiments of wave propagation in alternating porous layers saturated with either gas or water have shown that the mesoscopic loss mechanism can be significant in the seismic band, confirming the results obtained by White et al. (1975).This is a simple example of how microheterogeneities in the fluid and frame properties can affect observations at the macro scale. Similar results were presented by Carcione et al. (2003) and Helle et al. (2003) in partially saturated rocks in the high-frequency range.

The experiments show that the finite-element procedure employed is accurately representing the attenuation

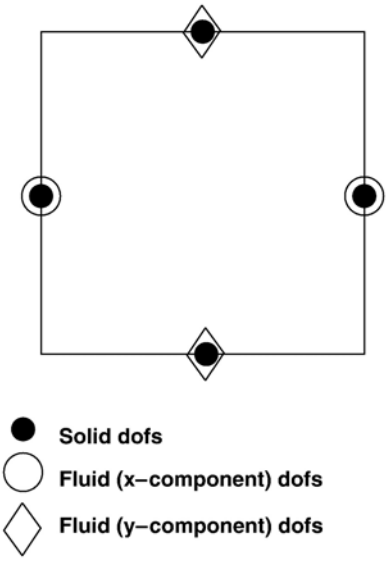


Fig. 8. Local degrees of freedom (*dofs*) associated with each component of the solid displacement and the fluid displacement vector.

effects, and could be used to analyze this phenomenon in highly heterogeneous porous materials, such as in the case of patchy saturation or fractal porosity–permeability distributions.

Acknowledgements

This work was partially funded by CONICET, Argentina (PIP 5126/05) and the Agencia Nacional de Promoción Científica y Tecnológica (ANPCyT), PICT 2003, #03-13376. The authors wish to thank William Whitson and Bryan Putnam from Purdue University Computing Center for their technical support.

Appendix A. Description of the numerical procedure

Here the finite-element spaces $\mathcal{NC}^h$ and $\mathcal{W}^h$, and the numerical procedure employed in the simulations are briefly described.

The finite-element spaces are defined locally on a reference square $\widehat{\mathrm{R}}=[-1,\ 1]^2$ as follows. For each component of the solid displacement, set

$$\widehat{\mathcal{NC}}(\widehat{R}) = \mathrm{Span}\{1, \hat{x}, \hat{y}, \alpha(\hat{x})-\alpha(\hat{y})\},$$
$$\alpha(\hat{x}) = \hat{x}^2-\frac{5}{3}\hat{x}^4,$$

with the degrees of freedom being the values at the midpoint of each edge of $\widehat{\mathrm{R}}$.

Next, for the fluid displacement vector, if $\psi^L(\hat{x}) = \frac{-1+\hat{x}}{2}, \psi^R(\hat{x}) = \frac{1+\hat{x}}{2}, \psi^B(\hat{y}) = \frac{-1+\hat{y}}{2}, \psi^T(\hat{y}) = \frac{1+\hat{y}}{2}$, let

$$\widehat{\mathcal{W}}(\widehat{R}) = \mathrm{Span}\{(\psi^L(\hat{x}),0)^t, (\psi^R(\hat{x}),0)^t, (0,\psi^B(\hat{y}))^t, (0,\psi^T(\hat{y}))^t\}.$$

Fig. 8 shows the local degrees of freedom (*dofs*) associated with each component of the solid displacement and the fluid displacement vector.

Now the finite-element spaces associated with the partition $\mathcal{T}^h$ are defined by scaling and translations in the usual fashion as follows. For each Ω_j, let $F_{\Omega j}: \widehat{\mathrm{R}}\to\Omega_j$ be an invertible affine mapping such that $F_{\Omega j}(\widehat{\mathrm{R}})=\Omega_j$, and define

$$\mathcal{NC}_j^h = \{\mathrm{v}=(\mathrm{v}_1,\mathrm{v}_2)^t : \mathrm{v}_i = \widehat{\mathrm{v}}_i\circ F_{\Omega_j}^{-1}, \widehat{\mathrm{v}}_i\in\widehat{\mathcal{NC}}(\widehat{R}), i=1,2\},$$
$$\mathcal{W}_j^h = \{w : w = \widehat{w}\circ F_{\Omega_j}^{-1}, \widehat{w}\in\widehat{\mathcal{W}}(\widehat{R})\}.$$

Setting

$$\mathcal{NC}^h = \{\mathrm{v} : \mathrm{v}_j = \mathrm{v}|_{\Omega_j}\in\mathcal{NC}_j^h, \mathrm{v}_j(\xi_{jk}) = \mathrm{v}_k(\xi_{jk})\forall(j,k)\},$$
$$\mathcal{W}^h = \{w\in H(\mathrm{div};\Omega) : w_j = w|_{\Omega_j}\in\mathcal{W}_j^h\},$$

the global finite-element space to approximate the solution u of Eq. (2.9) is defined by

$$\mathcal{V}^h = (\mathcal{NC}^h)^2\times\mathcal{W}^h.$$

Standard approximation theory implies that, for all $\varphi=(\varphi^{(1)},\ \varphi^{(2)})^{\mathrm{t}}\in[H^2(\Omega)]^2\times H^1(\mathrm{div};\Omega)$,

$$\inf_{p\in\mathcal{NC}^h}\left[\|\varphi^{(1)}-p\|_0 + h\left(\sum_j\|\varphi^{(1)}-p\|_{1,\Omega_j}^2\right)^{\frac{1}{2}}\right]\le Ch^2\|\varphi^{(1)}\|_2, \tag{A.1a}$$

$$\inf_{p\in\mathcal{W}^h}\|\varphi^{(2)}-p\|_0\le Ch\|\varphi^{(2)}\|_1, \tag{A.1b}$$

$$\inf_{p\in\mathcal{W}^h}\|\varphi^{(2)}-p\|_{H(\mathrm{div};\Omega)}\le Ch(\|\varphi^{(2)}\|_1 + \|\nabla\cdot\varphi^{(2)}\|_1). \tag{A.1c}$$

The following *a priori* error estimates for the procedure (3.1) has been presented by Santos and Sheen (in press).

Theorem A. 1. *Let $u=(u^s,\ u^f)\in\mathcal{V}$ and $u^h\in\mathcal{V}^h$ be the solutions of Eqs.* (2.9) and (3.1)*, respectively. We then have the following energy-norm error estimate: for sufficiently small $h>0$,*

$$\|u^s-u^{(s,h)}\|_{1,h} + \|\nabla\cdot(u^f-u^{(f,h)})\|_0 + |u^{(s)}-u^{(s,h)}|_{0,\Gamma} + |(u^f-u^{(f,h)})\cdot\nu|_{0,\Gamma}$$
$$\le C(\omega)h\left[\|u^s\|_2 + \|u^f\|_{\frac{3}{2}} + \|\nabla\cdot u^f\|_1\right].$$

As explained in Section 3, the algebraic problem associated with the global procedure (3.1) cannot be efficiently solved with iterative global solvers due to the large number of degrees of freedom needed to represent the mesoscopic loss mechanism. For this reason, the following iterative domain-decomposition algorithm was used in this work.

Set $\Gamma_j=\partial\Omega\cap\partial\Omega_j$, $\Gamma_{jk}=\partial\Omega_j\cap\partial\Omega_k$, and denote by ξ_j and ξ_{jk} the midpoints of Γ_j and Γ_{jk}, respectively. Let us denote by ν_{jk} the unit outer normal on Γ_{jk} from Ω_j to Ω_k and by ν_j the unit outer normal to Γ_j. Let χ_j and χ_{jk} be two unit tangents on Γ_j and Γ_{jk} so that $\{\nu_j,\ \chi_j\}$ and $\{\nu_{jk},\ \chi_{jk}\}$ are orthonormal systems on Γ_j and Γ_{jk}, respectively.

Consider the decomposition of problem (2.4) and (2.7) over Ω_j as follows: for $j=1,\ \ldots,\ J$, find $u_j(x,\ \omega)$ satisfying

$$-\omega^2\mathcal{P}u_j + i\omega\mathcal{B}u_j-\mathcal{L}(u_j) = F,\quad \Omega_j, \tag{A.2a}$$

$$\mathcal{G}_{\Gamma_{jk}}(u_j) + i\omega\beta_{jk}S_{\Gamma_{jk}}(u_j) = \mathcal{G}_{\Gamma_{kj}}(u_k)-i\omega\beta_{jk}S_{\Gamma_{kj}}(u_k),\quad \Gamma_{jk}, \tag{A.2b}$$

$$-\mathcal{G}_{\Gamma_j}(u_j) = i\omega\mathcal{D}S_{\Gamma_j}(u_j),\quad \Gamma_j, \tag{A.2c}$$

where $\mathcal{G}_{\Gamma_{jk}}$ and $\mathcal{G}_{\Gamma_j}$ are defined as in Eq. (2.5). Here β_{jk} is a positive definite matrix function defined on the interior boundaries Γ_{jk}. The Robin transmission conditions (A.2b) impose the continuity of the solid displacement, the normal component of the fluid displacement and the stresses at the interior interfaces Γ_{jk}.

Next, following Douglas et al. (1999) and Santos and Sheen (in press), let us introduce a set of Lagrange multipliers λ^h_{jk} associated with the values of the forces at the midpoints ξ_{jk} of Γ_{jk} in the sense that $\lambda^h_{jk} \sim \mathcal{G}_{jk}(u_j)(\xi_{jk})$. The Lagrange multipliers λ^h_{jk} belong to the following space of functions defined on the interior interfaces Γ_{jk}:

$$\Lambda^h = \{\lambda^h : \lambda^h|_{\Gamma_{jk}} = \lambda^h_{jk} \in [P_0(\Gamma_{jk})]^3 = \Lambda^h_{jk}, \forall\{j,k\}\},$$

where $P_0(\Gamma_{jk})$ denotes the constant functions on Γ_{jk}.

Moreover, for $\Gamma=\Gamma_j$ or $\Gamma=\Gamma_{jk}$ let $\langle\!\langle u, v\rangle\!\rangle_\Gamma$ denote the approximation of $\langle\cdot,\cdot\rangle_\Gamma$ by the mid-point quadrature: $\langle\!\langle u, v\rangle\!\rangle_\Gamma = (u, \bar{v})(\xi_{jk})|\Gamma|$ where $|\Gamma|$ is the measure of Γ.

The domain-decomposition iteration is defined as follows: For all $j=1, \ldots, J$ choose an initial guess $(u_j^{\{h,0\}}, \lambda_{jk}^{\{h,0\}}) \in \mathcal{N}C_j^h \times \mathcal{W}_j^h \times \Lambda_{jk}^h$. Then, for $n=1, 2, 3, \ldots$, and $j=1, \ldots, J$, compute $(u_j^{\{h,n\}}, \lambda_{jk}^{\{h,n\}}) \in \mathcal{N}C_j^h \times \mathcal{W}_j^h \times \Lambda_{jk}^h$ as the solution of the equations

$$\begin{aligned}
&-\omega^2(\mathcal{P}u_j^{\{h,n\}}, v)_j + i\omega(\mathcal{B}u_j^{\{h,n\}}, v)_j \\
&\quad + \sum_{l,m}(\sigma_{lm}(u_j^{\{h,n\}}), \varepsilon_{lm}(v^{(1)}))_j \\
&\quad - (p_f(u_j^{\{h,n\}}), \nabla\cdot v^{(2)})_j \\
&\quad + i\omega\langle \mathcal{D}S_{\Gamma_j}(u_j^{\{h,n\}}), S_{\Gamma_j}(v)\rangle_{\Gamma_j} \\
&\quad + \sum_k \langle i\omega\beta_{jk}\mathcal{S}_{\Gamma_{jk}}(u_j^{\{h,n\}}), \mathcal{S}_{\Gamma_{jk}}(v)\rangle_{\Gamma_{jk}} \\
&\quad = (F, v)_{\Omega_j} - \sum_k \langle i\omega\beta_{jk}S_{\Gamma_{jk}}(u_k^{\{h,n-1\}}), S_{\Gamma_{jk}}(v)\rangle_{\Gamma_{jk}} \\
&\qquad + \sum_k \langle\langle \lambda_{kj}^{\{h,n-1\}}, S_{\Gamma_{jk}}(v)\rangle\rangle_{\Gamma_{jk}}, \quad v \in \mathcal{N}C^h(\Omega_j)\times\mathcal{W}_j^h,
\end{aligned} \tag{A.3a}$$

$$\lambda_{jk}^{\{h,n\}} = \lambda_{kj}^{\{h,n-1\}} - i\omega\beta_{jk}[S_{\Gamma_{jk}}(u_j^{\{h,n\}}) + S_{\Gamma_{kj}}(u_k^{\{h,n-1\}})] \times(\xi_{jk}), \text{ on } \Gamma_{jk}, \forall k. \tag{A.3b}$$

Eq. (A.3b), used to update the Lagrange multipliers, is obtained directly from Eq. (A.2b) evaluated at the midpoint ξ_{jk}.

Eq. (A.3a) yields a 12×12 linear system of equations for the degrees of freedom associated with the vector displacements of the solid and fluid phases on each subdomain Ω_j at the n-iteration level. The iteration (A.3a)–(A.3b) is a Jacobi-type iteration that converges to the solution u^h of Eq. (3.1) (see Santos and Sheen, in press). A twice as fast iteration may also be defined by using a red–black type iteration (see Douglas et al., 2001; Ha et al., 2002; Santos and Sheen, in press). The iteration parameter matrix β_{jk} is chosen to have the same form of the matrix $\mathcal{D}$ in Eq. (2.7), with entries obtained by averaging the coefficients in the definition of the matrices $\mathcal{A}$ and $\mathcal{M}$ in Eq. (2.8) on both sides of the boundary Γ_{jk}.

The space–time solution is obtained by solving Eqs. (A.3a)–(A.3b) for a finite number of temporal frequencies and using an approximate inverse Fourier transform (Douglas et al., 1993).

Appendix B. Complex bulk modulus of a periodic system of porous layers

We consider a periodic layered system composed of porous media 1 and 2 with thickness d_l, $l=1$, 2 and period d_1+d_2. White et al. (1975) obtained the complex modulus for a P1 wave traveling along the direction perpendicular to the stratification. It is given by

$$E = \left[\frac{1}{E_0} + \frac{2(r_2-r_1)^2}{i\omega(d_1+d_2)(I_1+I_2)}\right]^{-1}, \tag{B.1}$$

where

$$E_0 = \left(\frac{p_1}{E_{G_1}} + \frac{p_2}{E_{G_2}}\right)^{-1}, \tag{B.2}$$

with $p_l=d_l/(d_1+d_2)$, $l=1$, 2. Omitting the subindex l for clarity, we have for each medium

$$E_G = K_c + \frac{4}{3}\mu, \tag{B.3}$$

where K_c is given by Eq. (2.2).

Moreover,

$$r = \frac{\alpha K_{av}}{E_G} \tag{B.4}$$

is the ratio of fast P wave fluid tension to total normal stress,

$$I = \frac{\eta}{\kappa k}\coth\left(\frac{kd}{2}\right) \tag{B.5}$$

is an impedance related to the slow P wave,

$$k = \sqrt{\frac{i\omega\eta}{\kappa K_E}} \tag{B.6}$$

is the complex wavenumber of the slow P wave, and

$$K_E = \frac{E_m K_{av}}{E_G}, \tag{B.7}$$

is an effective modulus, with

$$E_m = K_m + \frac{4}{3}\mu \tag{B.8}$$

the dry-rock fast P wave modulus.

Let us assume in the following analysis that the properties of the frame are the same in media 1 and 2 and that the contrast is due to two different saturating fluids (for example, water and gas). The approximate transition frequency separating the relaxed and unrelaxed states (i.e., the approximate location of the relaxation peak) is

$$f_m = \frac{8\kappa_1 K_{E_1}}{\pi\eta_1 d_1^2}, \tag{B.9}$$

where the subindex 1 refers to water for a layered medium alternately saturated with water and gas. At this reference frequency, the Biot slow-wave attenuation length equals the mean layer thickness or characteristic length of the inhomogeneities (Gurevich et al., 1997) (see below). Eq. (B.9) indicates that the mesoscopic-loss mechanism moves towards the low frequencies with increasing viscosity and decreasing permeability, i.e., the opposite behaviour of the Biot relaxation mechanism.

The mesoscopic mechanism is due to the presence of the Biot slow wave and the diffusivity constant is $\gamma = \kappa K_E/\eta$. The critical fluid-diffusion relaxation length L is obtained by setting $|kL| = 1$, where k is the wavenumber (Eq. (B.6)). It gives $L = \sqrt{\gamma/\omega}$. The fluid pressures will be equilibrated if L is comparable to the period of the stratification. For smaller diffusion lengths (e.g., higher frequencies) the pressures will not be equilibrated, causing attenuation and velocity dispersion. Notice that the reference frequency (Eq. (B.9)) is obtained for a diffusion length $L = d_1/4$.

At enough low frequencies, the fluid pressure is uniform (isostress state) and the effective modulus of the pore fluid is given by Wood's (1955) law:

$$\frac{1}{K_f} = \frac{p_1}{K_{f1}} + \frac{p_2}{K_{f2}}. \tag{B.10}$$

It can be shown (see Johnson, 2001) that $E(\omega = 0)$ is equal to the plane-wave modulus (Eq. (B.3)) for a fluid whose composite modulus is given by Eq. (B.10). On the other hand, at high frequencies, the pressure is not uniform but can be assumed to be constant within each phase. In such a situation Hill's (1964) theorem gives the high-frequency limit $E(\omega = \infty) = E_0$ (see Eq. (B.2)).

References

Biot, M.A., 1956a. Theory of propagation of elastic waves in a fluid-saturated porous solid. I. Low frequency range. J. Acoust. Soc. Am. 28, 168–171.

Biot, M.A., 1956b. Theory of propagation of elastic waves in a fluid-saturated porous solid. II. High frequency range. J. Acoust. Soc. Am. 28, 179–191.

Biot, M.A., 1962. Mechanics of deformation and acoustic propagation in porous media. J. Appl. Phys. 33, 1482–1498.

Carcione, J.M., 2001. Wave fields in real media: Wave propagation in anisotropic, anelastic and porous media. Handbook of Geophysical Exploration, vol. 31. Pergamon Press Inc.

Carcione, J.M., Helle, H.B., Pham, N.H., 2003. White's model for wave propagation in partially saturated rocks: comparison with poroelastic numerical experiments. Geophysics 68, 1389–1398.

Douglas Jr., J., Santos, J.E., Sheen, D., Bennethum, L., 1993. Frequency domain treatment of one-dimensional scalar waves. Math. Models Methods Appl. Sci. 3, 171–194.

Douglas Jr., J., Santos, J.E., Sheen, D., Ye, X., 1999. Nonconforming Galerkin methods based on quadrilateral elements for second order elliptic problems. RAIRO Math. Model. Numer. Anal. 33, 747–770 (M2AN).

Douglas Jr., J., Santos, J.E., Sheen, D., 2001. Nonconforming Galerkin methods for the Helmholtz equation. Numer. Methods Partial Differ. Equ. 17, 475–494.

Gassmann, F., 1951. Ü ber die elastizität poros¨er medien (On the elasticity of porous media). Vierteljahrsschr. Nat. Ges. Zur. 96, 1–23.

Gurevich, B., Zyrianov, V.B., Lopatnikov, S.L., 1997. Seismic attenuation in finely layered porous rocks: effects of fluid flow and scattering. Geophysics 62, 319–324.

Ha, T., Santos, J.E., Sheen, D., 2002. Nonconforming finite element methods for the simulation of waves in viscoelastic solids. Comput. Methods Appl. Mech. Eng. 191, 5647–5670.

Helle, H.B., Pham, N.H., Carcione, J.M., 2003. Velocity and attenuation in partially saturated rocks. Poroelastic numerical experiments. Geophys. Prospect. 51, 551–566.

Hill, R., 1964. Theory of mechanical properties of fiber-strengthened materials. J. Mech. Phys. Solids 11, 357–372.

Johnson, D.L., 2001. Theory of frequency dependent acoustics in patchy-saturated porous media. J. Acoust. Soc. Am. 110, 682–694.

Nedelec, J.C., 1980. Mixed finite elements in R^3. Numer. Math. 35, 315–341.

Picotti, S., Carcione, J.M., 2006. Estimating seismic attenuation (Q) in the presence of random noise. J. Seism. Explor. 15, 165–181.

Quan, Y., Harris, J.M., 1997. Seismic attenuation tomography using the frequency shift method. Geophysics 62, 895–905.

Raviart, P.A., Thomas, J., 1975. Mixed finite element method for 2nd order elliptic problems. Mathematical Aspects of the Finite Element Methods, Lecture Notes of Mathematics, vol. 606. Springer.

Santos, J.E., Corbero, J.M., Ravazzoli, C.L., Hensley, J.L., 1992. Reflection and transmission coefficients in fluid-saturated porous media. J. Acoust. Soc. Am. 91 (4), 1911–1923.

Santos, J.E., Sheen, D., in press. Finite Element Methods for the Simulation of Waves in Composite Saturated poroviscoelastic Media. SIAM J. Numer. Anal.

White, J.E., Mikhaylova, N.G., Lyakhovitskiy, F.M., 1975. Low-frequency seismic waves in fluid-saturated layered rocks. Izvestija Academy of Sciences USSR. Phys. Solid Earth 10, 654–659.

Wood, A.W., 1955. A Textbook of Sound. MacMillan Co.

Zyserman, F.I., Gauzellino, P.M., Santos, J.E., 2003. Dispersion analysis of a non-conforming finite element method for the Helmholtz and elastodynamic equations. Int. J. Numer. Methods Eng. 58, 1381–1395.